Research Article

For reprint orders, please contact: reprints@futuremedicine.com

Nanomedicine

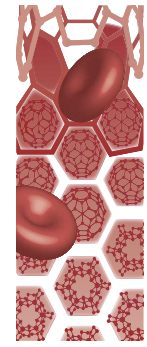

Lignin-graft-PLGA drug-delivery system improves efficacy of MEK1/2 inhibitor in triple-negative breast cancer cell line

C Ethan Byrne[1], Carlos E Astete[1], Manibarathi Vaithiyanathan[2], Adam T Melvin[2], Mahsa Moradipour[3], Stephen E Rankin[3], Barbara L Knutson[3], Cristina M Sabliov[1] & Elizabeth C Martin*[,1]

[1]Department of Biological & Agricultural Engineering, Louisiana State University, LA 70803, USA

[2]Cain Department of Chemical Engineering, Louisiana State University, LA 70803, USA

[3]Department of Chemical & Materials Engineering, University of Kentucky, KY 40506, USA

*Author for correspondence: emart93@lsu.edu

Aim: Few targeted therapies are available for triple-negative breast cancer (TNBC) patients. Here, we propose a novel alkaline-lignin-conjugated-poly(lactic-*co*-glycolic acid) (L-PLGA) nanoparticle drug delivery system to improve the efficacy of targeted therapies. **Materials & methods:** L-PLGA nanoparticles (NPs) loaded with the MEK1/2 inhibitor GDC-0623 were characterized, tested *in vitro* on MDA-MB-231 TNBC cell line and compared with loaded PLGA NPs. **Results:** Loaded L-PLGA NPs were less than half the size of PLGA NPs, had slower drug release and improved the efficacy of GDC-0623 when tested *in vitro*. We demonstrated that GDC-0623 reversed epithelial-to-mesenchymal transition in TNBC. **Conclusion:** Our findings indicate that L-PLGA NPs are superior to PLGA NPs in delivering GDC-0623 to cancer cells for improved efficacy *in vitro*.

Graphical abstract:

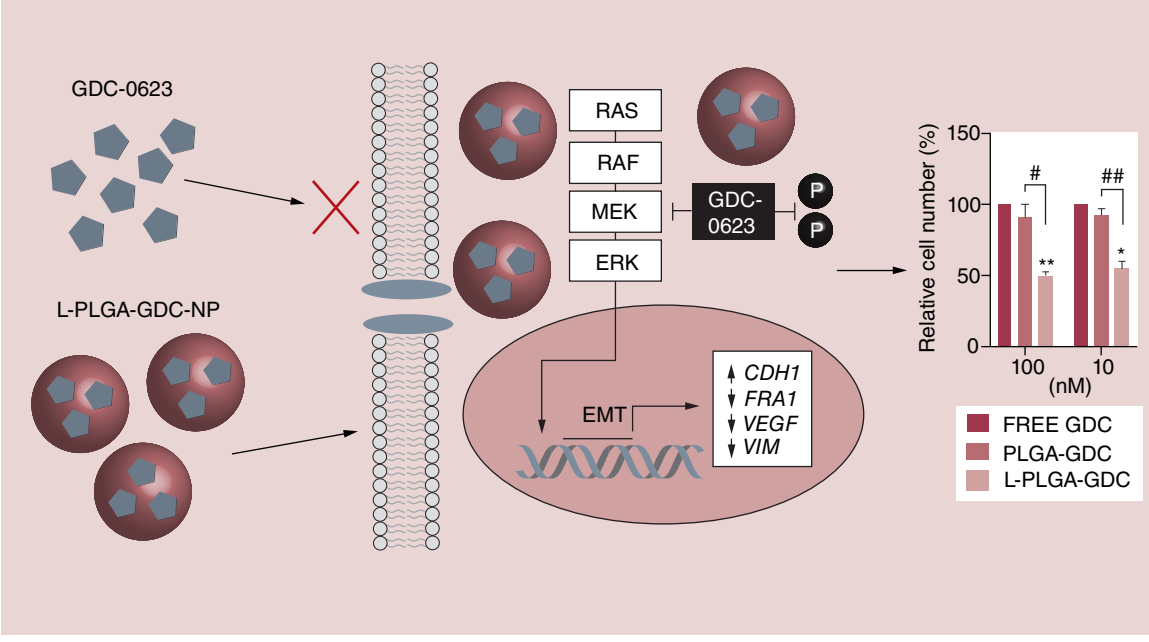

First draft submitted: 8 January 2020; Accepted for publication: 19 February 2020; Published online: 2 April 2020

Keywords: breast cancer • drug delivery • lignin • nanoparticle • targeted therapies • triple-negative

Future Medicine

It is estimated that one in eight women in the USA will develop invasive breast cancer throughout the course of their lives while more than 40,000 women die from it annually [1]. Of all breast cancers, 10–15% will be triple-negative breast cancer (TNBC), lacking the estrogen, progesterone and human EGF receptor (HER). TNBC is associated with a worse prognosis than hormone receptor-positive breast cancers, particularly in the first 5 years after diagnosis [2]. Hormone receptor positive and HER2 (HER2/neu) amplified cancers have a mechanism for intervention where targeted therapies can bind the receptors in an antagonistic manner that prevent the activation of proliferation and survival pathways in the cancer cells [3]. TNBC lacks both estrogen receptor and HER2, resulting in no available target for therapy. Patients with TNBC also typically have a higher grade of disease and often experience an early pattern of recurrence [4]. Because TNBCs lack drug-targetable estrogen receptors and HER2, it usually necessitates adjuvant therapy, such as chemotherapy [4]. Chemotherapy often induces co-morbidities such as peripheral neuropathy, febrile neutropenia and cardiovascular disease [5–7]. The morbidity that occurs with systemic cytotoxic chemotherapy [8], coupled with the physical and emotional pain from mastectomy, leaves much to be desired in the way we currently treat TNBC; it creates a need for the development of new targeted therapies and better drug delivery methods. Unlike radiation and chemotherapies, targeted therapies can selectively act on cancer cells while sparing normal tissues and having minimal cytotoxic effects [9]. These therapies can work on specific molecular targets or they can be designed to only interact with a selected target. Examples of these therapies include hormone therapies, signal transduction inhibitors, gene expression modulators, apoptosis inducers, angiogenesis inhibitors, immunotherapies and toxin delivery molecules [10–12].

One such targeted cancer therapy is the MEK1/2 inhibitor GDC-0623, which was used in Phase I of clinical trials in patients with advanced solid tumors [13]. MEK is part of the RAS-RAF-MEK-MAPK/ERK signaling cascade (Figure 1) and it is responsible for activating ERK1/2 through phosphorylation [14]. In this pathway, RAS initiates growth-factor-mediated signal transduction across the cell membrane by assembling transient signaling complexes that induce transcription, which alters cell morphology, migration, cell survival, proliferation and even senescence [15]. In human tumors, roughly 20% have mutations that activate RAS genes, making RAS a prime target for intervention. However, development of a successful inhibitor of RAS has thus eluded researchers [16,17]. GDC-0623 is a promising inhibitor in the RAS-RAF-MEK-MAPK/ERK signaling cascade by targeting of MEK1/2 through phosphorylation inhibition of ERK1/2 [18]. In breast cancer, metastatic risk and drug resistance increases with activation of the RAS-RAF-MEK-MAPK/ERK signaling cascade [19,20]. Also, a more metastatic phenotype, which is associated with more aggressive and deadly breast cancer subtypes, has been correlated with increased expression of the RAS isoform, KRAS [21]. Although GDC-0623 was well tolerated and showed dose-proportional and time-dependent pharmacokinetic characteristics in a Phase I trial, there was no accumulation at steady-state following daily oral dosing because of its short half-life of 4–6 h [13]. Using a drug-delivery system to slowly release GDC-0623 could help to overcome its short half-life.

Unfortunately, failure in Phase I occurs with many experimental compounds, including targeted therapies, and only 10% of compounds in Phase I are likely to gain the US FDA approval [22]. Failure may be due to poor water solubility, low retention time in blood circulation, inability to selectively target tumor cells and lack of tissue penetration [23]. Targeted therapies may have poor efficacy when the target of the drug is internal and the drug molecule is not readily taken up by the cell [24]. Nanoparticle drug-delivery systems (NPDDS) can be used to overcome these hurdles by allowing for controlled release of drugs that can be varied depending on the characteristics of system, active targeting by attaching ligands to the particle, passive targeting through enhanced permeation and retention effects, and overcoming pharmacokinetic limitations associated with conventional drug formulations [25–28]. NPDDS deliver their chemical payloads to the tumor with the goal of mitigating the effects of the cancer-fighting agents on the rest of the body [29]. Drug delivery to the tumor can be achieved by passive and active targeting; however, active targeting cannot be achieved without the passive phenomenon of the enhanced permeability and retention (EPR) effect [30]. Passive targeting takes advantage of the development of new, leaky vasculature that tumor growth induces in response to the increased metabolic demand of the growing tumor [31]. Nanoparticles (NPs) in the range of 20 to 200 nm can exit the leaky vasculature from the blood stream into the tumor and accumulate inside the interstitial space [29]. Once inside the tumor, these NPs are retained there because the poorly formed vasculature is inefficient at removing them, thus producing the EPR effect [32,33]. EPR allows NPs to localize in the tumor and then release their chemical payload. The NPs may be taken up by the cells, depending on the characteristics of the NPs, where they can release their chemical payload directly into the cells [34].

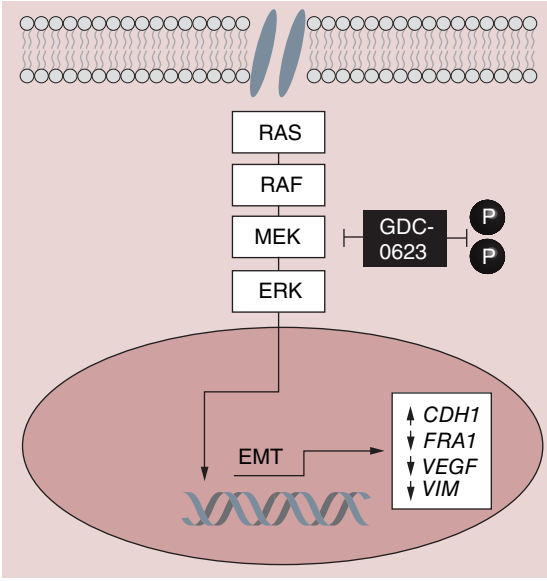

Figure 1. Transcriptional targets of MEK. EMT genes *CDH1*, *FRA1*, *VEGF* and *VIM* are under transcriptional control of ERK1/2. GDC-0623 inhibits phosphorylation of ERK1/2, which leads to upregulation of *CDH1* and downregulation of *FRA1*, *VEGF* and *VIM*.

Despite the advantages of NPs, there can still be issues with their cell uptake. Lignin is a biopolymer found in plant cell walls that has been shown to improve NPDDS uptake when conjugated to another compound [35,36]. In one such example, a polymeric NPDDS was improved when alkaline lignin (AL) was conjugated to folic acid-polyethylene glycol (FA-PEG) polymer and loaded with the targeted cancer therapy hydroxyl camptothecin (HCPT) to form FA-PEG-AL/HCPT NPs [36]. HCPT is a DNA topoisomerase I inhibitor [37]. When FA-PEG-AL/HCPT particles were compared with free HCPT, the particles demonstrated a sevenfold increase in blood circulation time and fivefold increase in cellular uptake [36].

To address the issue of poor pharmacokinetics of GDC-0623, we propose using a novel AL-graft-poly(lactic-*co*-glycolic acid) (L-PLGA) NPDDS loaded with GDC-0623. The goal of the L-PLGA NPDDS is to slow the release of the drug and to enhance NP uptake by cells for an increased local drug concentration inside the cells and improved activity in TNBC.

Materials & methods

Dichloromethane (DCM), dimethyl sulfoxide (DMSO), dimethylformamide (DMF), ethyl acetate, ethyl ether, acetonitrile (ACN), oxalyl chloride and tetramethylrhodamine isothiocyanate (TRITC), 12,000–14,000 MW membrane, 12–14 kDa dialysis tubing, Dulbecco's modified Eagle's medium, HyClone Cosmic Calf Serum, Gibco Minimum Essential Medium amino acids (MEM AA), Gibco MEM nonessential amino acids (NEAA), Gibco sodium pyruvate, Gibco antibiotic–antimycotic, 96-well Corning Costar tissue culture plastic plates, Corning 10-cm tissue culture-treated dishes, Corning T25 tissue culture-coated flask, mammalian protein extraction reagent (M-PER), protease inhibitor, phosphatase inhibitor, Invitrogen Bolt $4\frac{1}{2}$% Bis-Tris Plus electrophoresis gels, 10% formalin solution were obtained from Thermo Fisher Scientific (MA, USA). PLGA (50:50, 38–54 kDa), trifluoroacetic acid (TFA), *N*-Boc-ethylenediamine, 1-(bis[dimethylamino]methylene)-1H-1,2,3-triazolo(4,5-b)pyridinium 3-oxid hexafluorophosphate, recombinant human insulin were obtained from Sigma-Aldrich (MO, USA). AL was obtained from TCI chemicals. 1,2-Dipalmitoyl-*sn*-glycero-3-phosphocholine (DPPC) was obtained from Avanti Polar Lipids (AL, USA). Primary antibodies used p44/42 MAPK (ERK1/2) and phosphor-p44/42 MAPK (ERK1/2) were obtained from Cell Signaling Technology (MA, USA). Secondary antibodies IR-tagged were obtained from LiCor Biosciences (NE, USA). Qiagen RNeasy Kit were obtained from Qiagen (Hilden, Germany). qScript cDNA SuperMix and PerfeCTa SYBR® Green SuperMix were obtained from Quantabio (UT, USA). 1.5 Coverglass bottom cell-imaging dishes were obtained from MatTek Corporation (MA, USA). All chemicals were reagent grade.

10.2217/nnm-2020-0010

Synthesis of lignin-PLGA biopolymer

The synthesis involves two steps based on PLGA acylation. The first step was the PLGA chlorination performed in a three-neck 500-ml round-bottom flask under mild stirring. The reaction was under nitrogen gas bubbler connected to a wash bottle with sodium hydroxide solution to trap hydrogen chloride formed during synthesis. The dissolution of 1 g of PLGA in 20 ml of DCM was performed at room temperature under mild stirring for 20 min. An excess of oxalyl chloride (5 eq.) was slowly added to PLGA solution with further addition of DMF. The solution was cooled down to 4°C during addition. The reaction was completed at room temperature in 4 h. Finally, the polymer was precipitated and washed with ethyl ether twice. The modified PLGA polymer was vacuum dried overnight.

The second step performed allowed attachment of the activated PLGA to AL at a mass ratio of AL to PLGA of 1:2 w/w. Dry lignin (500 mg) was dissolved in 20 ml of DMSO at room temperature under mild mixing. Next, 1 g of PLGA-Cl was dissolved in 20 ml of DMSO, and it was slowly added to the lignin solution. The reaction was performed at room temperature and stopped after 24 h. The biopolymer lignin-PLGA was washed three-times with cold water and ether to remove the unreacted lignin. The biopolymer was dried under high vacuum overnight. The synthesized L-PLGA biopolymer was stored at -20°C for further characterization and NPs synthesis.

Synthesis of TRITC-labeled PLGA & lignin-PLGA

PLGA-TRITC and L-PLGA-TRITC fluorescent NPs were synthesized for the NP uptake study. All other particles were synthesized for the *in vitro* drug studies. Conjugation of TRITC to PLGA was performed by dissolving 2 g of PLGA in 30 ml of DCM at room temperature and further addition of 104 mg of 1-(bis[dimethylamino]methylene)-1H-1,2,3-triazolo(4,5-b)pyridinium 3-oxid hexafluorophosphate, 46.8 mg of *N*-Boc-ethylenediamine and 0.4 ml of *N,N*-diisopropylethylamine. After 12 h of stirring at room temperature, the reaction was stopped by the addition of 150 ml of distilled water. Next, precipitation of the polymer was performed by addition of 200 ml of ethanol to obtain a white solid. The washing protocol was repeated twice, and the solids were dried under high vacuum overnight. The deprotection step was performed with 1 g of solids by resuspending the intermediate product in 20 ml of DCM with further addition of 20 ml of TFA (1:1 DMC:TFA v/v). After 35 min at room temperature under mild stirring, the reaction was stopped by precipitation in ethyl ether (200 ml). The activated polymer (PLGA-amine) was dried under high vacuum overnight.

The final step was the conjugation of PLGA-amine to TRITC. The dissolution of PLGA-amine polymer (1000 mg) in 30 ml of DCM and 0.075 ml of triethylamine was performed at room temperature. After 15 min of mixing at room temperature, 25 mg of TRITC was added. The reaction was carried out overnight at room temperature. Finally, the organic phase was washed with water five-times in a separation funnel. The PLGA-TRITC polymer was precipitated out by adding ethanol (150 ml) to obtain and dark pink solid. The solids were dried under high vacuum for 2 days and stored at -20°C for further use in NPs synthesis [38].

For TRITC-L-PLGA synthesis, 1 g of L-PLGA was dissolved in 30 ml of DCM and 20 mg of TRITC was added. The reaction was performed at room temperature for 24 h. Finally, the TRITC-L-PLGA was precipitated in ethyl ether following the same protocol described for TRITC-PLGA.

PLGA, PLGA-GDC & PLGA-TRITC NP synthesis

PLGA NPs as a control, PLGA NPs with GDC-0623 entrapped (PLGA-GDC NPs) and PLGA NPs with TRITC covalently attached (PLGA-TRITC NPs) for visualization of cellular uptake were synthesized by emulsion evaporation technique. In general, 300-mg PLGA polymer (for PLGA-TRITC NPs, a 1:1 mass ratio with PLGA was used) was dissolved in 6 ml of ethyl acetate. When required, 12 mg of the drug GDC-0623 was added in the organic phase with an organic phase of 25% acetone and 75% ethyl acetate. The aqueous phase was prepared by dissolving 270 mg of Tween 80 in 60 ml of deionized (DI) water. The organic phase was poured in the aqueous phase under stirring. The emulsion obtained was run through a microfluidizer (Microfluidics, MA, USA) four-times at 30,000 psi. Next, a rotary evaporator (Buchi Corporation, DE, USA) was used to evaporate the solvent under vacuum. After the evaporation, the volume was adjusted by adding 6.5 ml of 2% w/v polyvinyl alcohol (PVA) and stirred for 20 min. Finally, trehalose was added (1–1 mass ratio) to freeze dry (Labconco, MO, USA) the NP samples for 2 days. The lyophilized samples were stored at 4°C.

L-PLGA, L-PLGA-GDC & L-PLGA-TRITC NP synthesis

The L-PLGA NPs as a control, alkaline-lignin-conjugated PLGA NPs with GDC-0623 entrapped (L-PLGA-GDC NPs) and alkaline-lignin-conjugated PLGA NPs with TRITC covalently attached L-PLGA-TRITC NPs) were synthesized by emulsion evaporation technique. Briefly, 400 mg of L-PLGA polymer was dissolved in 6 ml of ethyl acetate. The GDC-0623 drug (14 mg) loaded L-PLGA NPs were added in the organic phase. The organic phase for the synthesis of fluorescent NPs used a mass ratio of 1:3 (PLGA-TRITC to L-PLGA polymers). The mixtures were mixed for 30 min at room temperature. The organic phase for L-PLGA-GDC NPs was formed the same as PLGA-GDC NPs described above. The aqueous phase for all L-PLGA NPs was 60 ml of low resistivity water. The aqueous and organic phases were combined and run through the microfluidizer (Microfluidics) as described above. The solvent was evaporated with a rotavapor (Buchi Corporation) for 1 h at 35°C. Finally, 450 mg of trehalose was mixed into the aqueous suspension and freeze dried with a 2.5-l FreeZone (Labconco). The lyophilized NPs were stored at 4°C for further characterization.

NP size measurements

The synthesized NPs were characterized by measuring size, polydispersity index (size distribution) and ζ potential with dynamic light scattering (DLS) technique using a Malvern Zetasizer Nano ZS (Malvern Instrument Ltd, Worcestershire, UK). Samples were measured after resuspension in DI water.

NP morphology

The transmission electron microscopy (TEM) pictures were taken with a JEOL JEM 1400 (Jeol USA Inc., MA, USA). First, the polymeric NPs were resuspended in DI water at a final concentration of 2 mg/ml. A sample droplet was mixed with uracil acetate (2%; contrast agent) and placed on a carbon grid. The excess was removed from the carbon grid and let dried for 15 min at room temperature before the grid was placed in the TEM.

NP stability

L-PLGA NPs were resuspended in 1× phosphate-buffered saline (PBS; pH 7.4) at a concentration of 1 mg/ml and incubated at 37°C while shaking. Samples were collected at 0, 8, 24, 48, 72, 96 and 120 h. NPs were characterized by measuring size and ζ potential with DLS technique using a Malvern Zetasizer Nano ZS (Malvern Instrument Ltd).

Quantification of GDC-0623 by HPLC

The detection and quantification of GDC-0623 was performed by HPLC Agilent 1200 (Agilent, CA, USA). The column was Zorbax Eclipse XDB C-18 (3 × 150 mm, 3.5 µm). ACN and water were used with a gradient mobile-phase elution. The gradient was as follow: the flow was 5% ACN from 0 to 20 min, from 20 to 21 min it was increased to 80% ACN, from 21 to 26 min it was increased to 95% ACN and from 26 to 27 min, the ACN was decreased to 5%. The injection volume was 10 µl with a flow rate of 1 ml/min. The DAD signal was set at 260 and 280 nm. The elution time was 10.3 min for GDC-0623.

Entrapment efficiency

Entrapment efficiency (EE) was determined by HPLC. A known mass of GDC-0623-loaded particles was dissolved in ACN and analyzed by HPLC. The following equation (Equation 1) was used to determine EE:

$$EE = \frac{mass\ of\ drug\ in\ NPs}{mass\ of\ initial\ drug} \times 100 \qquad \text{(Eq. 1)}$$

Quartz crystal microbalance with dissipation

The interaction of PLGA and L-PLGA NPs with DPPC-supported lipid bilayers (SLBs) was studied using a quartz crystal microbalance with dissipation monitoring (QCM-D; Q-sense E4, Biolin Scientific, Sweden) in a PBS solution (pH of 7.4) at 20°C. The changes in resonance frequency (Δf) and energy dissipation (ΔD) of the sensor were recorded with time over the processes of creating a SLB, flowing NPs over the bilayer and rinsing the bilayer, as described below. The lipid bilayer was developed on an oxidized gold QCM-D substrate (Nanoscience Instruments, AZ, USA) by solvent-assisted lipid bilayer formation, as described by Tabaei *et al.* [39]. PBS solution was flowed through the QCM-D cell for 5 min, followed by isopropanol for 15 min, all at a flowrate of 30 ml/h.

Then, a DPPC lipid solution in isopropanol (1.5 mg/ml) was passed over the sensor for 60 min. Lastly, the sensor was washed with PBS again, resulting in the rearrangement of the lipid adsorbed on the sensor into a SLB [40–42]. In the next step of the experiment, suspensions of PLGA and L-PLGA NPs in PBS at two different concentrations (0.1 and 1 mg/ml) were passed over the lipid bilayer at a flowrate of 24 ml/h. Prior to suspending the NPs in PBS, dialysis using a 12,000–14,000 MW membrane was employed to remove trehalose from the lyophilized particles. After flowing NPs suspension over the SLB on the QCM sensor, the surface was rinsed with PBS for 75 min to remove particles unattached to the surface. The mass of lipid bilayer per area ($\Delta m/A$) was measured from the change in frequency (Δf) of the sensor using the Sauerbrey equation (Equation 2), which assumes that the layer is thin and rigid, and has previously been used before to determine the mass of the lipid bilayers formed on QCM sensors [41,43,44]:

$$\frac{\Delta m}{A} = \frac{c\,\Delta f}{n_r} \qquad \text{(Eq. 2)}$$

where C is the material specific Sauerbrey constant (17.7 ng cm^{-2} Hz^{-1}), and n is the overtone number at which the frequency is being measured [45]. The magnitude of the overtone is inversely proportional to the distance from the surface being probed; the third overtone is measuring mass changes further from the surface than the seventh overtone [46]. Here, we report Δf and ΔD at the third overtone (n = 3), a standard practice in the QCM literature [42,47]. In pure water, the depth of penetration is approximately 145 nm for the third overtone [43,48]. The thickness of a hydrated phospholipid bilayer is approximately 8 nm (much less than the penetration depth; $d/\lambda_3 = 0.055$), so the Sauerbrey equation is expected to be valid [43,49].

Release profile of GDC-0623 from PLGA & L-PLGA NP

PLGA NPs and L-PLGA NPs with entrapped drug were resuspended in 1× PBS at a concentration of 9.8 and 5.9 mg/ml, respectively. The resuspended NPs were dialyzed with 1× PBS while shaking at 37°C. Dialysis tubing was 12–14 kDa. Samples were collected from inside the dialysis bags at specified time points over 48 h. The PBS was changed twice daily. Samples collected were dissolved in ACN and analyzed using HPLC.

Cell culture

Breast cancer cell line MDA-MB-231 was generously donated by the Burow Lab at Tulane University School of Medicine. Cells were maintained in 5% CO_2 at 37°C and cultured with Dulbecco's modified Eagle's medium supplemented with 10% Hyclone Cosmic Calf Serum, 50 ng/ml insulin and 1% MEM AA, MEM NEAA, sodium pyruvate and antibiotic–antimycotic.

Cell survival assay

MDA-MB-231 breast cancer cell line was seeded at a density of 5×10^3 cells per well in cell culture medium on 96-well Corning Costar tissue culture plastic plates. After 24 h in culture, cells were treated with vehicle control (DMSO), PLGA NPs (negative control), L-PLGA NPs (negative control), free GDC-0623 (positive control), PLGA-GDC NPs and L-PLGA-GDC NPs. Cells were treated with 100 and 10 nM doses of GDC in either free on NP entrapped form. After treatment, cells were cultured for 5 days and then stained with crystal violet. Crystal violet was eluted with 33% acetic acid and absorbance was measured at 570 nm using a BioTek Cytation 3 plate reader (BioTek Instruments Inc., VT, USA). The experiment was carried out with internal replicates n = 3 and biological replicates of n = 3.

Western blot

MDA-MB-231 breast cancer cells were seeded at a density of 2×10^6 cells per 10-cm tissue culture-treated dish. After 24 h, cells were treated with DMSO (vehicle), free GDC-0623, PLGA-GDC NPs or L-PLGA-GDC NPs. Cells were treated with a 1-nM dose of GDC in either free or NP entrapped form and cultured for 24 h. All samples were washed with PBS and collected on ice for total protein extraction. Protein was extracted with lysis cocktail of m-PER supplemented with protease inhibitor (0.1%), and phosphatase inhibitor (0.1%). Total protein was loaded for all samples. Samples were prepared for electrophoresis and run at 150 V on Invitrogen Bolt $4\frac{1}{2}$% Bis-Tris Plus electrophoresis gels per manufacturer's specifications. Protein was transferred to iBlot 2 Transfer Stack using Invitrogen iBlot 2 Gel Transfer Device (Thermo Fisher Scientific, MA, USA) per manufacturer's specifications.

Samples were blocked in 3% milk for 1 h. Primary antibodies used p44/42 MAPK (ERK1/2) and phosphor-p44/42 MAPK (ERK1/2) were diluted 1:1000 and secondary antibodies IR-tagged were diluted 1:10,000 in 5% BSA-TBST. Western blots were analyzed using LiCor Odyssey Infrared Imaging System. Biological replicates were n = 3.

Cell morphology

Cells were seeded and treated in the same manner as the cell survival assay. After staining with crystal violet, the cells were imaged at 20x using Nikon Eclipse Ti2.

Quantitative RT-PCR

MDA-MB-231 cells were seeded on Corning T25 flasks at a density of 500,000 cells per flask in culture medium. After 24 h in culture, cells were treated with vehicle (DMSO), 1 nM free GDC-0623 (positive control), PLGA-GDC NPs and L-PLGA-GDC NPs and collected at 24 h post-treatment. Total RNA was isolated from cell using Qiagen RNeasy Kit. 1 µg total RNA was used to generate cDNA with the qScript cDNA SuperMix cDNA synthesis kit as per manufacturer's protocol. Gene expression analysis was run with PerfeCTa SYBR® Green SuperMix. Total gene expression analysis was done through the ΔΔCt (fold expression) method. Data were normalized to *PPIB* housekeeping gene with biological triplicates ± SEM, n = 3.

Cellular uptake of PLGA & L-PLGA NP

MDA-MB-231 breast cancer cells were seeded on 35 mm, 1.5 coverglass bottom, cell imaging dishes. Cells were seeded at a density of 45×10^3 cells/dish and cultured for 24 h. TRITC NPs were applied to cells at 0.1 mg/ml concentration for 3 h. Cells were washed three-times with PBS, fixed with 10% paraformaldehyde (PFA) and stained with 4′,6-diamidino-2-phenylindole (DAPI) according to manufacturers' protocol and imaged with Nikon Eclipse Ti2 with NIS Elements AR software (Nikon Inc., NY, USA). 2 × 2 binning was used to increase signal-to-noise ratio of TRITC signal.

TRITC NP standard curve to quantify cellular uptake

To quantify the uptake of TRITC NPs by the cancer cells, standard curves for the TRITC NPs were generated. PLGA-TRITC and L-PLGA-TRITC NPs were resuspended in 1× PBS at a concentration of 1 mg/ml to make stock solutions. The stock solutions were used to make serial dilutions ranging from 0.5 to 0.01 mg/ml. Samples of the dilutions were loaded in triplicate into 96-well plates. Fluorescence was measured at 553/627 nm using a BioTek Cytation 3 plate reader (BioTek Instruments Inc.). Excel was used to generate the standard curve of fluorescence intensity at known concentrations.

NP uptake analyzed by flow cytometry

MDA-MB-231 breast cancer cells were seeded in T25 cell culture flasks at a density of 5×10^5 cells per flask. After 24 h, they were either untreated (control) or treated with 0.1 mg/ml TRITC NPs for 0.5, 1.5 and 3 h. Cells were collected using EDTA in PBS, fixed with 10% formalin and stored in PBS. Samples were analyzed using a FACS Aria Fusion cell sorter (Becton-Dickinson, NJ, USA). The mean fluorescence intensity of 10,000 events was measured per sample. The autofluorescence of the control was subtracted from the other samples and equations from the standard curves were used to calculate the mean concentration of NPs in the cells.

Results

NP characterization

The goals of this study were to compare the efficacy of entrapped the MEK1/2 inhibitor GDC-0623 to free GDC-0623 and to compare L-PLGA NPDDS to PLGA NPDDS. PLGA is an established biomaterial for NPDDSs, PLGA NPs were used as a benchmark for the L-PLGA-based NPs. Three types of particles containing either PLGA or L-PLGA were synthesized and characterized: TRITC-conjugated fluorescent NPs (for uptake study), empty NPs (negative control) and NPs with entrapped drug. The NPs were characterized in terms of average diameter, polydispersity index, zeta potential (ζ) and drug EE (Table 1). All three versions of PLGA-based NPs had similar characteristics (201–223 nm in diameter and ζ of -30 to -38 mV). Overall, the L-PLGA-based NPs were much smaller than the PLGA-based NPs. The EE of GDC-0623 in PLGA NPs was slightly higher than L-PLGA NPs at 74 and 67%, respectively. The L-PLGA-based NPs were not all similar; L-PLGA-TRITC yielded much larger NPs

Table 1. Nanoparticle characterization.

NP	Diameter (nm)	PDI	ζ potential (mV)	EE (%)	TRITC (μg/mg NPs)
PLGA-TRITC	222 ± 2	0.088 ± 0.014	-36.6 ± 1.4	n/a	0.56 ± 0.011
L-PLGA-TRITC	169 ± 16	0.206 ± 0.018	-70.1 ± 2.0	n/a	0.20 ± 0.004
PLGA	223 ± 1	0.044 ± 0.004	-30.4 ± 0.1	n/a	n/a
L-PLGA	92 ± 3.7	0.089 ± 0.014	-52.0 ± 3.3	n/a	n/a
PLGA-GDC	201 ± 2.5	0.109 ± 0.017	-37.6 ± 0.9	74 ± 1.4	n/a
L-PLGA-GDC	78 ± 4	0.091 ± 0.014	-48.1 ± 3.2	67 ± 2.3	n/a

EE: Entrapment efficiency: L-PLGA-GDC: Alkaline-lignin-conjugated-poly(lactic-*co*-glycolic acid) GDC-0623; n/a: Not applicable; NP: Nanoparticle; PDI: Polydispersity index; TRITC: Tetramethylrhodamine isothiocyanate.

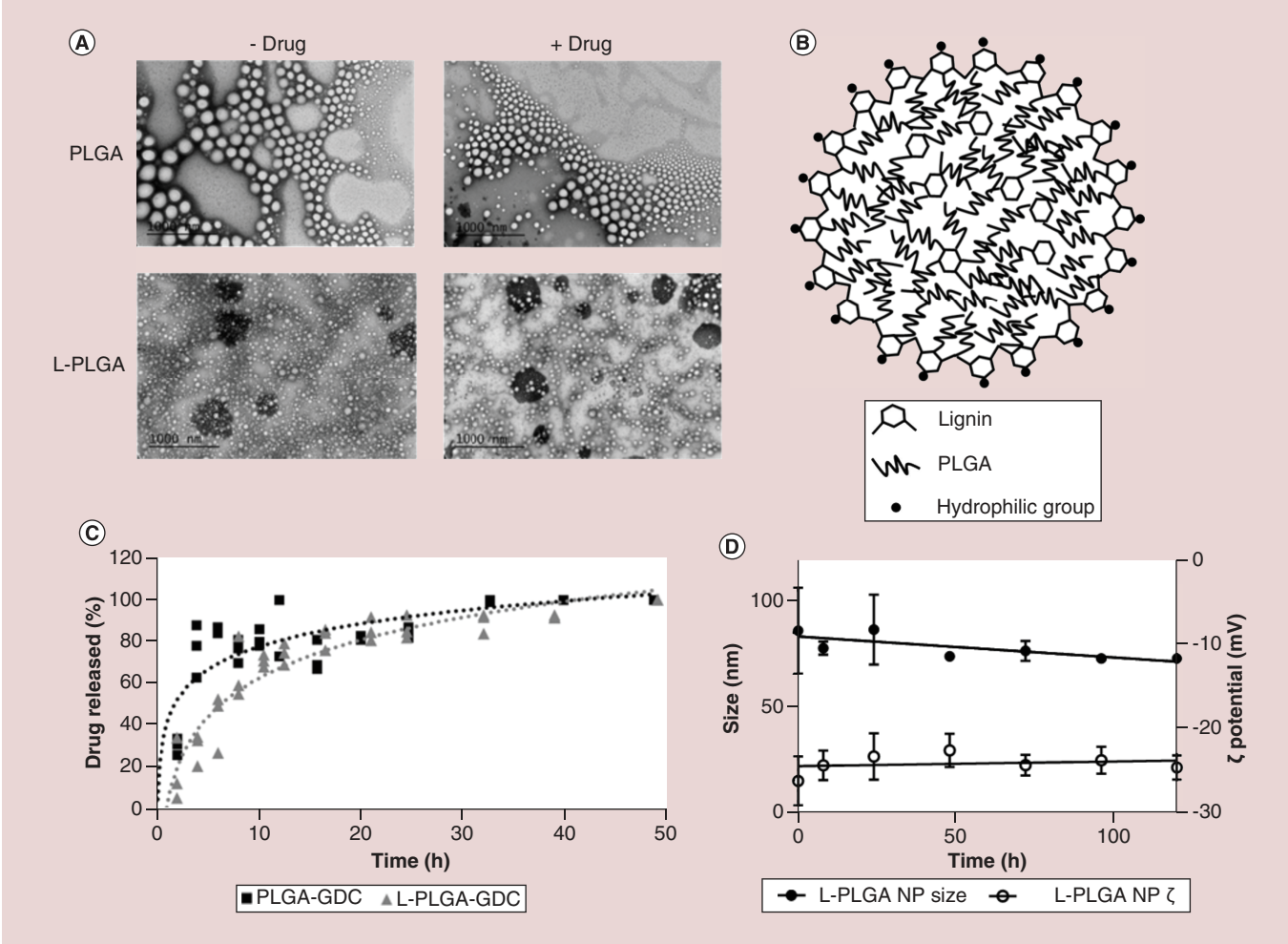

Figure 2. Lignin improves nanoparticle size and delays release of GDC-0623. (A) Transmission electron microscopy images of PLGA and lignin-conjugated PLGA with and without entrapped MEK inhibitor GDC-0623. Scale bar is 1000 nm. **(B)** Schematic of L-PLGA NP with hydrophobic core and hydrophilic shell. **(C)** Release profile of GDC-0623 from PLGA and L-PLGA NPs quantified with HPLC. Experiment was carried out in triplicate. **(D)** Size and ζ potential stability of L-PLGA in physiological conditions over 5 days. Error bars represent standard deviation.
L-PLGA NP: Alkaline-lignin-conjugated-poly(lactic-*co*-glycolic acid) nanoparticle.

(169 ± 16 nm) than L-PLGA (92 ± 3.7 nm) and L-PLGA-GDC NPs (78 ± 4 nm). The L-PLGA-TRITC NPs also had a much more negative ζ (-70.1 ± 2.0 mV relative to -52.0 ± 3.3 mV for L-PLGA NPs).

Illustrated in Figure 2 is the size and drug-release differences between PLGA and L-PLGA NPs. The size of the empty NPs (-drug) is similar to that of the loaded particles (+drug), while it is clear that the PLGA and PLGA-GDC

NPs (223 ± 1, 201 ± 2.5 nm) are much larger than the L-PLGA and L-PLGA-GDC NPs (92 ± 3.7, 78 ± 4 nm) (Figure 2A). The surfactant layer surrounding the PLGA-based NPs that prevents them from agglomerating is visible in the TEM images (Figure 2A). L-PLGA NPs also have a core–shell structure (Figure 2B). The hydrophilic moieties of lignin polymer assemble on the surface of the particle where they interact with the water forming the shell. The hydrophobic PLGA forms the core of the particles. When loaded with GDC-0623, both delivery systems exhibit a burst release initially followed by a more sustained release (Figure 2C). However, the L-PLGA NPs have a slower release; PLGA-GDC NPs and L-PLGA-GDC NPs released nearly all of the drug around 32 and 48 h, respectively. When tested for stability at physiological conditions, the L-PLGA NPs remained stable in size and zeta potential over 5 days (Figure 2D). There was a slight reduction in average particle size from 86.1 ± 20.4 nm at t = 0 h to 73.0 ± 1.8 nm at t = 120 h. The ζ potential changed slightly from -26.3 ± 2.9 to -24.7 ± 1.4 mV over 120 h.

QCM-D measurements of SLBs interactions with NPs

Adherence of NPs to cell membranes is an initial step in the process leading to NP uptake or toxicity [50,51]. Synthetic phospholipid bilayers, such as those comprising DPPC, in the form of solution-based vesicles or lipid bilayers on a solid support are frequently used as model cell membranes to interpret the interactions of cells with surfaces [52,53]. By forming a bilayer directly on a coated quartz crystal sensor, QCM-D has been used to investigate the adherence and uptake of NPs to SLBs [54], the structural rearrangement of NPs adsorbed to the SLBs [55], and the disruption of bilayers by NPs [56–58]. Here, the potential interactions of the cells with PLGA and L-PLGA NPs are inferred from the NP's ability to adhere to or to disrupt the SLBs on QCM gold sensors.

As interpreted from the Sauerbrey equation (Equation 2), the mass of the bilayer formed on a sensor is proportional to the decrease in an oscillating crystal's resonance frequency (Δf) [41,43,44]. The QCM-D response of the energy dissipation (ΔD) describes the variation in the viscoelasticity or rigidity of the film coated on the surface [57]. High values of dissipation are the result of deformation of a soft film, whereas low dissipation describes films that are nondeformable and rigid. In relation to SLBs, an increase in dissipation indicates the loosening or thickening of the lipid bilayer [46,59]. In the presence of NPs, an increase in dissipation suggests that the particles have adhered to the bilayer, leading to hydrodynamic effects that increase dissipation loss with the surrounding medium [60].

In Figure 3, we illustrate the typical frequency and dissipation profiles during the synthesis of an SLB using the solvent-assisted lipid bilayer formation method [61]. The time axis in Figure 3 progresses from flowing PBS over the sensor, then isopropanol, followed by a DPPC-isopropanol solution and finally back to PBS. It is this final step that allows the lipids adsorbed to the sensor to rearrange into a bilayer [39], as indicated by a sharp increase in frequency and a decrease in dissipation. The mass of the SLB formed on the sensor was measured from the frequency change between the initial PBS baseline (t = 5 min) and the baseline in PBS after SLB formation (t = 150 min) using the Sauerbrey equation (Equation 2). The lipid bilayer mass for all SLBs in this work was above 350 ng/cm^2, which is consistent with the reported mass for a lipid bilayer that is rigid and strongly coupled to the sensor [42,62,63]. Representative changes in frequency and dissipation are reported following the injection of PLGA and L-PLGA NPs (0.1 and 1 mg/ml) into the QCM cell containing the SLB (Figure 4). In these figures, NP injection begins at time zero and the corresponding value of Δf is set to zero for the fully formed bilayer. The change in frequency due to NP interactions is normalized by the absolute value of the frequency of the corresponding bilayer to account for the variation in the mass of bilayer formed by the SLB method. A common type of NP-bilayer interaction, adherence of the NPs to the SLBs, is suggested by the decreasing frequency (increasing mass; Figure 4A & C) and increasing dissipation (decreasing adsorbed layer rigidity; Figure 4B & D) over the timeframe (75 min) that L-PLGA is flowed into the QCM cell. At low particle concentration, rinsing with PBS appears to remove some adhered NPs (decreasing the mass). In contrast, the NPs deposited from the more concentrated solution appear to rearrange on the film surface during rinsing, resulting in a more hydrated film.

The PLGA NP-bilayer interactions, as interpreted from QCM-D, are distinctly different from those of L-PLGA. Upon injection of the PLGA NPs at both concentrations (0.1 mg and 1 mg/ml), a decrease in frequency (suggesting adherence of the NPs to the bilayer) followed by an increase in frequency (suggestion removal of NPs and/or bilayer mass) is observed (Figure 4A). At the higher NP concentration, the final Δf indicates that the particles disrupted and removed some of the model cell membrane. At low NP concentrations, the accumulation of more mass in the bilayer coupled with the presence of a minimum in frequency suggests that mass loss due to particles and/or bilayer removal occurs later in the injection. At both NP concentrations, with exposure of the bilayer to PLGA NPs, the dissipation increases and then stays constant upon rinsing, which suggests that the PLGA NPs form a less

10.2217/nnm-2020-0010

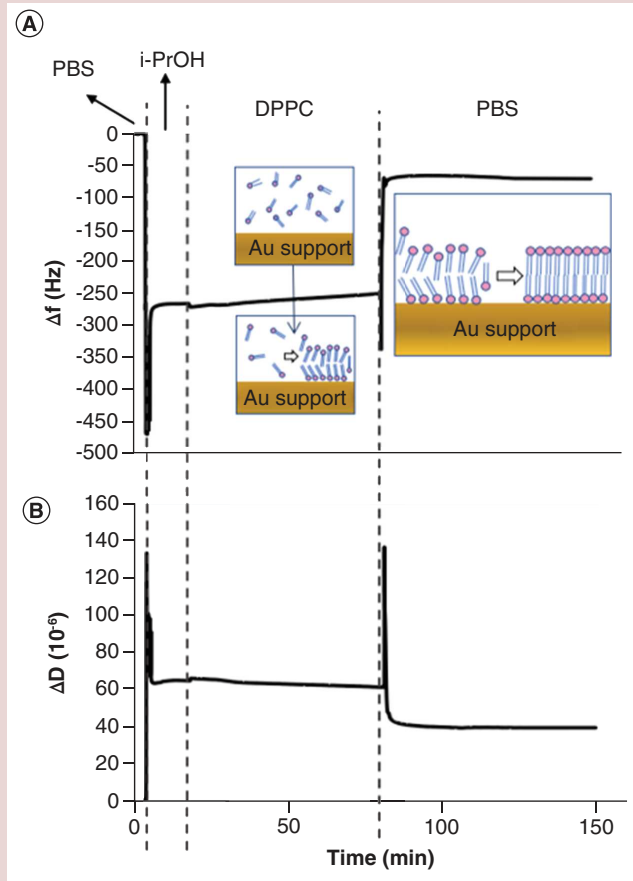

Figure 3. Synthesis of mimetic cell membrane quartz crystal microbalance with dissipation monitoring model. DPPC lipid bilayer is formed on Au-coated quartz crystals monitored by Quartz crystal microbalance with dissipation monitoring **(A)** frequency shifts and **(B)** dissipation shifts. The parts of the graphs separated by the dashed lines indicate the injection of PBS, isopropanol ('i-PrOH'), lipid mixture (1.5 mg/ml DPPC lipid in isopropanol, 'DPPC') and finally PBS.
DPPC: 1,2-Dipalmitoyl-sn-glycero-3-phosphocholine; PBS: Phosphate-buffered saline.

rigid structure when adsorbed to the lipid membrane or in the process of removing it (Figure 4A & B). Both the kinetics of adsorption of NPs and their ability to disrupt SLBs are a strong function of concentration [47,56–58], with faster adherence to lipid bilayers and disruption occurring at higher NP concentrations. In particular, a critical NP concentration may be required to observe disruption and removal of the lipid bilayer by QCM-D [58]. These results suggest a concentration of 1 mg/ml of PLGA NPs is above the critical NP concentration for bilayer disruption.

While the L-PLGA NPs adhered to the model cell membranes, PLGA NPs caused membrane disruption and removal. The distinctly different behaviors of PLGA NPs and L-PLGA NPs with SLBs may be related to the difference in their size as well as surface properties. Larger polymeric NPs are more likely to be engulfed by a bilayer than smaller NPs, leading to mass loss and membrane disruption upon removal [57]. Thus, the smaller size of L-PLGA NPs (92 ± 3.7 nm) compared with PLGA (223 ± 1 nm) would favor their penetration into the lipid bilayer rather than disruption [64,65]. Similarly, the effect of functionalized PLGA NPs size on their uptake by Caco-2 cells, a human colon adenocarcinoma cell line, is observed to be 1.3-fold greater for 100 nm NPs compared with 500-nm particles, and about 1.8-fold greater compared with 1000-nm particles [64]. Additionally, the surface chemistry of the polymeric NPs may play a role in the nature of their interaction with the lipid membranes. L-PLGA NPs are stabilized by surface AL, whereas PLGA NPs are stabilized by the addition of PVA, which may impact interactions with lipid bilayers [66].

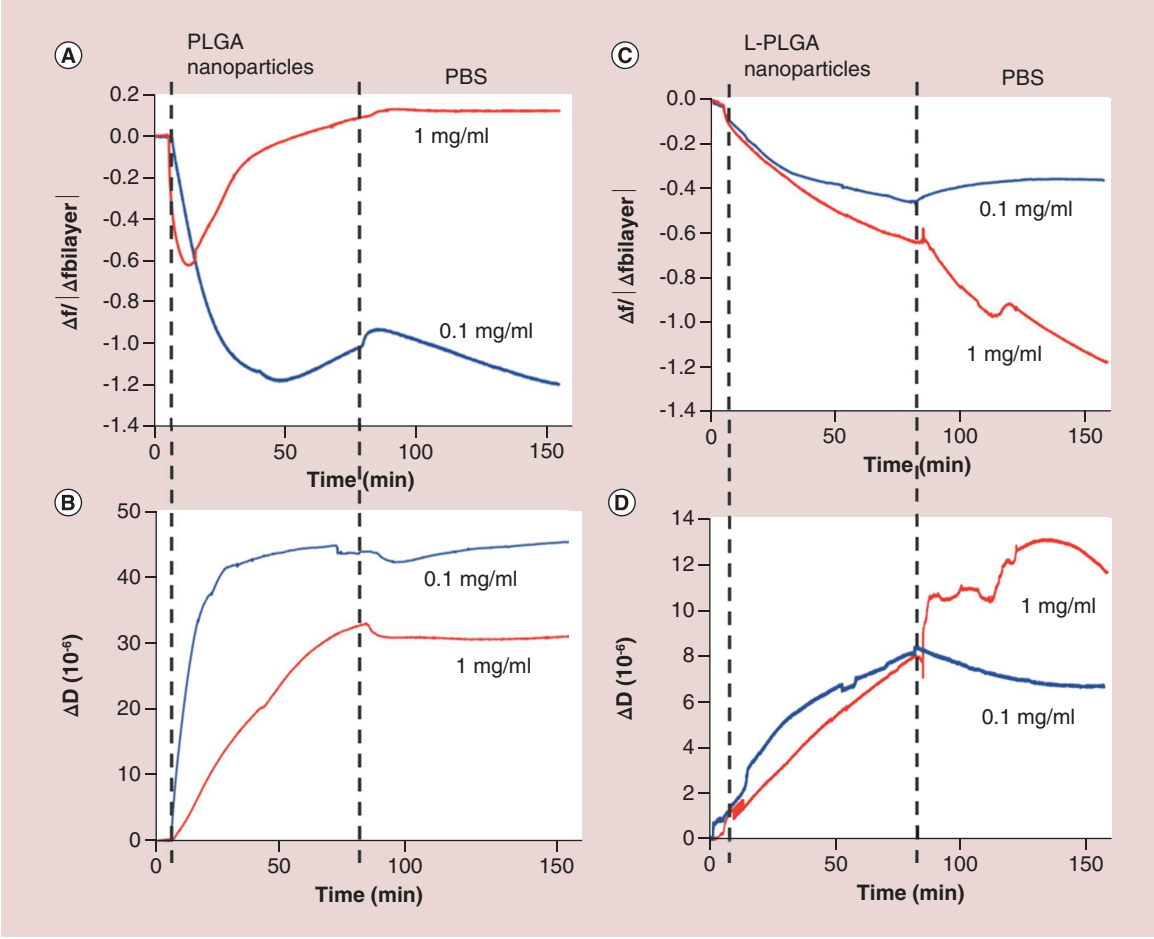

Figure 4. Quartz crystal microbalance with dissipation monitoring measurements of nanoparticle interactions with mimetic cell membranes. (A) Change in frequency and **(B)** change in dissipation with the introduction of PLGA nanoparticles (NPs) at 0.1 mg/ml (blue) and 1 mg/ml (red) on supported 1,2-dipalmitoyl-sn-glycero-3-phosphocholine (DPPC) lipid bilayers on a gold Quartz crystal microbalance sensor. **(C)** Change in frequency and **(D)** change in dissipation with the introduction of L-PLGA NPs at 0.1 mg/ml (blue) and 1 mg/ml (red) on supported DPPC lipid bilayers on a gold Quartz crystal microbalance sensor. Time is measured from particles injection onto an existing bilayer ('nanoparticles'), followed by the PBS buffer rinse ('PBS'). The x-axis (time) is set to a value 0 when the NPs are introduced to the fully formed DPPC bilayer. The y-axes in **(A)** and **(C)** are also normalized by dividing Δf by change in frequency corresponding to the DPPC SLB.
L-PLGA: Alkaline-lignin-conjugated-poly(lactic-*co*-glycolic acid); PBS: Phosphate-buffered saline.

In vitro drug study

Before we began the *in vitro* drug study (Figure 5), we needed to determine the optimal dose of GDC-0623 for MDA-MB-231 breast cancer cells. We screened GDC-0623 at five concentrations ranging from 10 μM to 1 nM (Figure 5A). When we compared the results with DMSO (vehicle), we observed significant reductions in cell numbers at 10 μM, 1 μM and 100 nM, but not at 10 and 1 nM. At 100 nM concentration, a 50% reduction in cell numbers was observed and hence deemed the optimal dose moving forward. Next, L-PLGA-GDC NPs were compared against negative controls (DMSO, PLGA NPs and L-PLGA NPs) and positive controls (free GDC-0623 and PLGA-GDC NPs; Figure 5B). The PLGA and L-PLGA negative controls did not reduce the relative number of cells, which indicated that the NPs themselves were not cytotoxic. Conversely, the number of cells treated with the negative NP controls actually increased slightly.

At 10 nM GDC 0623, PLGA-GDC NPs and free GDC-0623 had a similar effect on cell viability compared with DMSO control. Only L-PLGA-GDC was able to induce a significant reduction in cell numbers at 10 nM dose compared with DMSO control (Figure 5B). When compared with free GDC-0623, PLGA-GDC NPs were not significantly different from free GDC-0623, while L-PLGA-GDC demonstrated a significant reduction in cell

10.2217/nnm-2020-0010

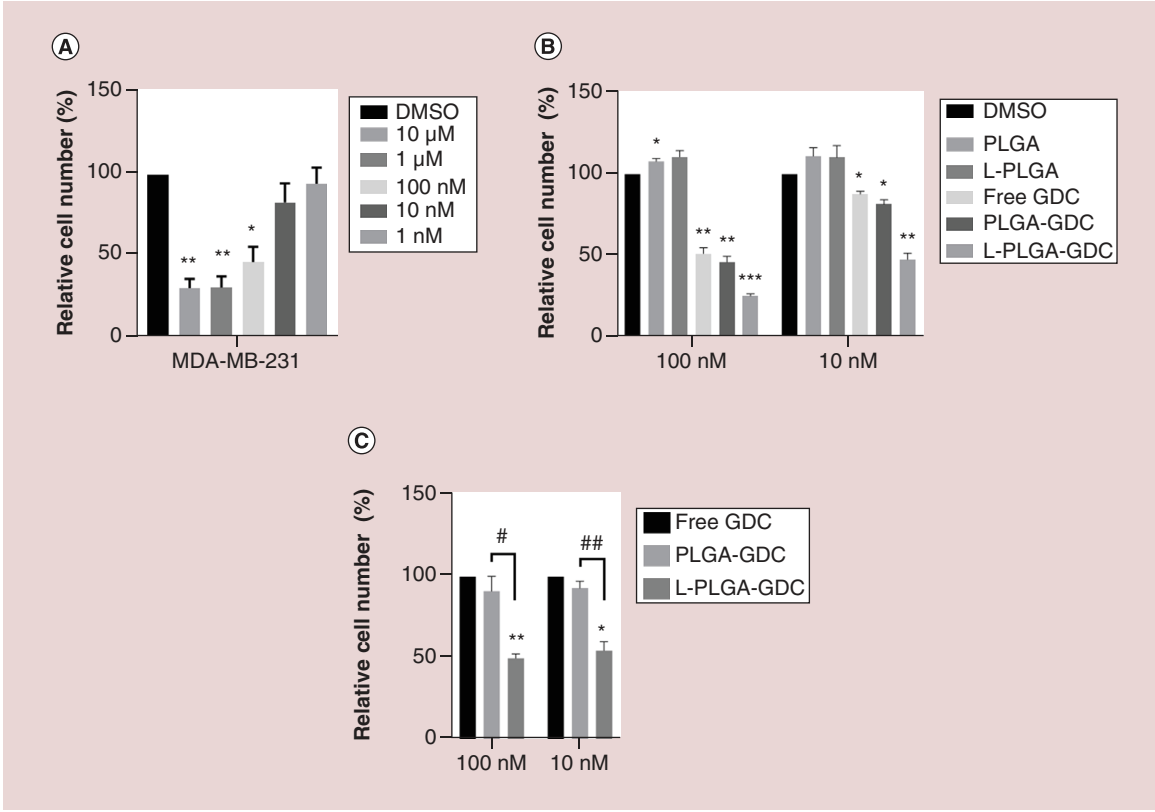

Figure 5. Alkaline-lignin-conjugated-poly(lactic-*co*-glycolic acid) nanoparticles improve efficacy of GDC-0623. (A) Dose response curve of MDA-MB-231 breast cancer cell line when treated with DMSO (vehicle) and GDC-0623 concentrations ranging from 10 μM to 1 nM. **(B)** MDA-MB-231 cell line treated with DMSO (vehicle), PLGA NPs (negative control), L-PLGA NPs (negative control), free GDC-0623 (positive control), PLGA NPs with entrapped GDC-0623 and L-PLGA NPs with entrapped GDC-0623 using drug concentration of 100 and 10 nM. Results were normalized to vehicle. **(C)** Results of NPs with entrapped drug normalized to free drug. Cells were treated for 5 days then stained with crystal violet. Crystal violet was eluted with 33% acetic acid and the absorbance was read at 570 nm. Error bars represent SEM; n = 3.
*p ≤ 0.05; **p ≤ 0.01; ***p ≤ 0.001; #p ≤ 0.05, ##p ≤ 0.01.
GDC: MEK1/2 inhibitor GDC-062; L-PLGA NP: Alkaline-lignin-conjugated-poly(lactic-co-glycolic acid) nanoparticle.

numbers (~50%) compared with both the free GDC-0623 and PLGA-GDC NPs at 10 and 1 nM (Figure 5C). These results indicated that L-PLGA-GDC NPs improved the efficacy of GDC-0623 at lower doses that were not found to be significant in the dosing curve of free GDC; PLGA-GDC NPs did not confer the same effect at the lower dose.

Western blots were performed to determine if the L-PLGA-GDC NPs could improve GDC-0623's inhibition of p-ERK1/2 compared with free GDC-0623 and PLGA-GDC NPs (Figure 6). When normalized to DMSO, all treatments were able to reduce p-ERK1/2 while there was no change in total ERK1/2 for any treatment group (Figure 6A & B). L-PLGA-GDC NPs significantly lowered p-ERK1/2 compared with free GDC and PLGA (Figure 6A & C).

While conducting these studies, we observed that cells treated with GDC-0623 had distinctive morphological differences suggestive of a mesenchymal-to-epithelial transition (MET) phenotype (Figure 7). This phenotype was most obvious in cells treated with L-PLGA-GDC NPs compared with vehicle-treated controls (Figure 7A). To determine if MEK1/2 inhibition induced a biological change in cancer cell phenotype, MDA-MB-231 cells treated with GDC-0623 were next evaluated for phenotypic changes and alterations of gene expression associated with the MEK pathway. qPCR was conducted to investigate the possibility of GDC-0623 reversing epithelial-to-mesenchymal transition (EMT) through the inhibition of MEK/ERK1/2-regulated genes *CDH1*, *VIM*, *FRA1* [67–69]. qPCR demonstrated that only L-PLGA-GDC NPs had a significant increase (16 ± 2.8-fold) in expression of the epithelial marker *CDH1* compared with vehicle control (Figure 7B). Additionally, L-PLGA NPs demonstrated

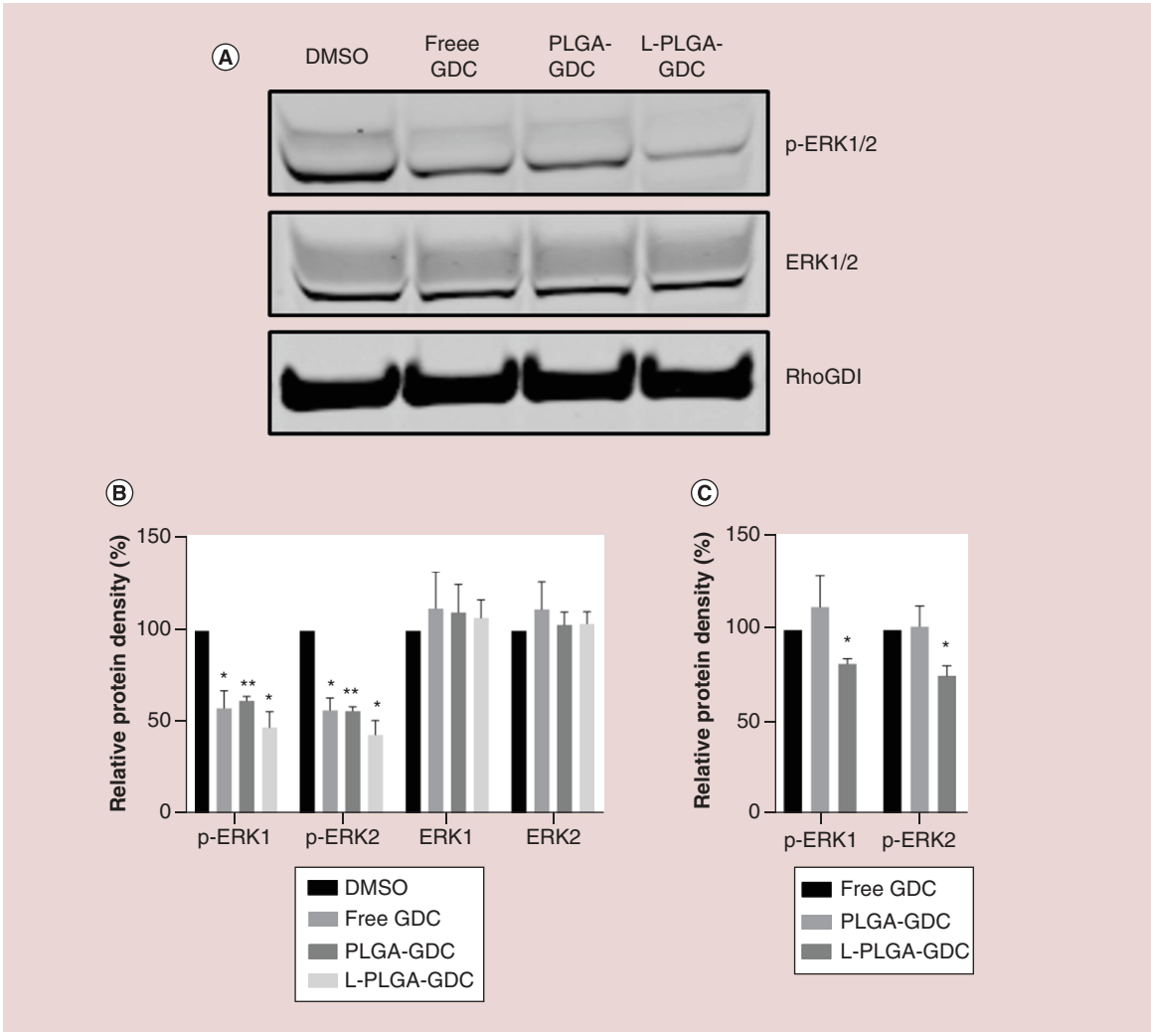

Figure 6. Alkaline-lignin-conjugated-poly(lactic-*co*-glycolic acid) nanoparticles improve phosphorylation inhibition of GDC-0623. MDA-MB-231 cell line was treated with DMSO (vehicle), free GDC-0623 (positive control), PLGA NPs with entrapped GDC-0623, and L-PLGA NPs with entrapped GDC-0623. **(A)** Images of western blot with RhoGDIα control. Western blot results normalized to **(B)** DMSO and **(C)** free GDC-0623. GDC-0623 concentration of 1 nM was used for all western blots. Error bars represent SEM; n = 3.
*$p \leq 0.05$; **$p \leq 0.01$.
DMSO: Dimethyl sulfoxide; GDC: MEK1/2 inhibitor GDC-062; L; L-PLGA NP: Alkaline-lignin-conjugated-poly(lactic-*co*-glycolic acid) nanoparticle.

a more significant reduction in expression of EMT-related genes *FRA1* (0.65 ± 0.03-fold), *VEGF* (0.30 ± 0.5-fold) and *VIM* (0.38 ± 0.10-fold) than the other treatments when compared with vehicle control (Figure 7C). Data normalized to free GDC-0623 (Figure 7D) demonstrated that L-PLGA-GDC NPs significantly increased expression of *CDH1* and reduced expression of *VEGF* and *VIM* compared with free GDC-0623 and PLGA-GDC NPs.

NP uptake

To confirm the prediction of the QCM-D model that L-PLGA NPs would interact with cell membranes which could lead to uptake by the cells, we conducted a cellular uptake study (Figure 8). MDA-MB-231 cells were treated with 0.1 mg/ml PLGA-TRITC and L-PLGA-TRITC NPs for 3 h and imaged using an inverted fluorescence microscope (Figure 8A). To quantitate the uptake, we made a standard curve with TRITC NPs (Figure 8B & C) and then performed a flow cytometry analysis (Figure 8D). The cells were again treated with the same concentrations of NPs, but the analysis was done at three time points of 0.5, 1.5 and 3 h to profile the uptake. The mean fluorescence

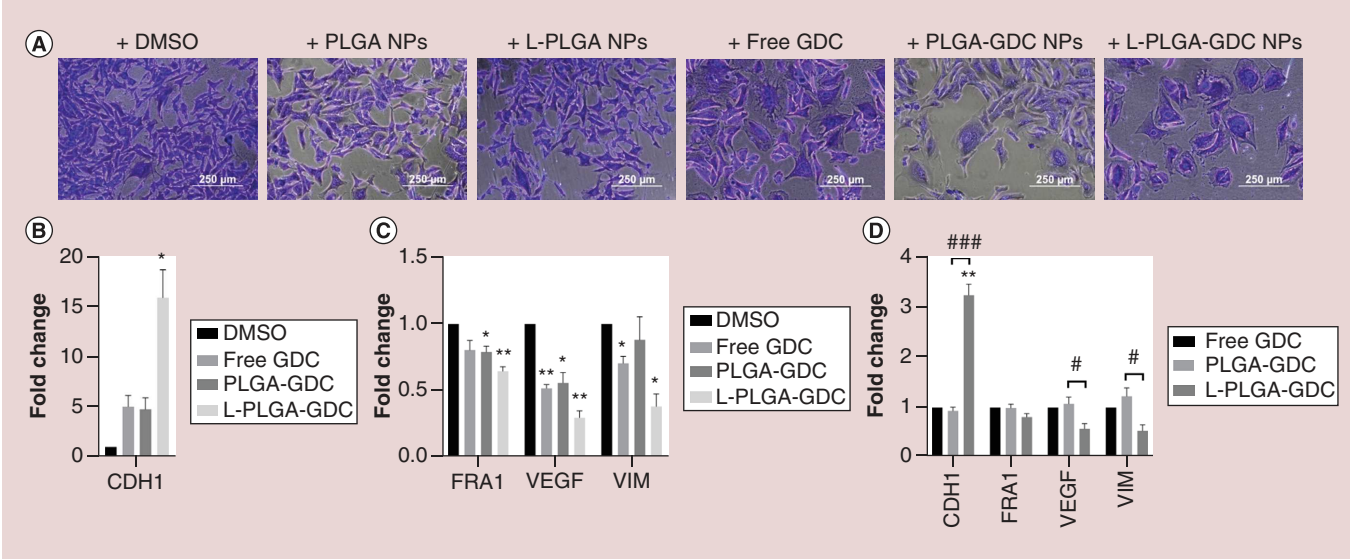

Figure 7. GDC-0623 reverses epithelial-to-mesenchymal transition in MDA-MB-231 cell line. MDA-MB-231 cell line was treated with DMSO (vehicle), free GDC-0623 (positive control), PLGA NPs with entrapped GDC-0623 and L-PLGA NPs with entrapped GDC-0623. **(A)** Morphology images of MDA-MB-231 cell line treated with DMSO, L-PLGA NPs (negative control), free GDC-0623 (positive control) and L-PLGA NPs with entrapped GDC-0623. qPCR results for EMT markers normalized to DMSO for **(B)** CDH1 and **(C)** FRA1, VEGF and VIM and **(D)** results normalized to free GDC-0623. GDC-0623 concentration of 1 nM for qPCR and 100 nM for morphology. Error bars represent SEM; n = 3. Scale bar is 250 µm.
*p ≤ 0.05; **p ≤ 0.01; #p ≤ 0.05, ###p ≤ 0.001.
DMSO: Dimethyl sulfoxide; EMT: Epithelial-to-mesenchymal transition; GDC: MEK1/2 inhibitor GDC-062; L; L-PLGA NP: Alkaline-lignin-conjugated-poly(lactic-*co*-glycolic acid) nanoparticle.

intensity was determined using 10,000 events (gating and sort data available in Supplementary Figure 1). There was an increase in NP uptake for both samples over the 3 h period, but the L-PLGA-TRITC NPs had a much greater uptake (Figure 8C). This increased uptake agrees with the QCM-D modeling.

Discussion

Through the use of our novel NPDDS, we have enhanced intracellular drug delivery of a targeted therapy to TNBC cells. Our characterization of the NPs demonstrated that L-PLGA was better suited for drug delivery. When tested as a negative control, both PLGA and L-PLGA were shown to be nontoxic with a slight increase in cell numbers (Figure 5B). We believe that the increase was due to the trehalose cryoprotective being a minor source of carbohydrates for the cells. L-PLGA NPs being much smaller than PLGA NPs makes them a more desirable NPDDS because a greater percentage of the L-PLGA NPs fall into the 20 to 200 nm range for passive targeting based on the EPR effect. The size of the PLGA NPs is largely a function of the surfactant, PVA. A smaller PLGA NP can be achieved when using surfactants that have a greater surface tension reduction than PVA [70], but we prefer PVA because of its biocompatibility [71]. The L-PLGA NPs did not require a surfactant to stabilize the particles. However, the conjugation of TRITC to the L-PLGA created a larger, more negative particle than L-PLGA-GDC (Table 1), but we believe it was an appropriate model to verify cellular uptake for the following reasons. First, the size of the particles was measured by DLS and it is the average size of the particles. There is a range of particle sizes and there is significant overlap of L-PLGA-GDC and L-PLGA-TRITC particle sizes (Supplementary Figure 2). Second, smaller particles have better cellular uptake than larger particles [64,72]. Therefore, given that the TRITC particles are larger, we can deduce that the smaller L-PLGA-GDC particles will have an even better cellular uptake than that observed for the TRITC labeled particles. The slower release of GDC-0623 from the L-PLGA-GDC NPs is also important for improving drug efficacy because GDC-0623 was excreted quickly form the body preventing drug accumulation at steady state. This slower release profile can be attributed to the presence of lignin on the surface of the L-PLGA-GDC NPs (Figure 2B). The L-PLGA NPs also proved to be quite stable in physiological conditions for extended periods of time with minimal change in size and zeta potential suggesting they would be appropriate for use in an animal model.

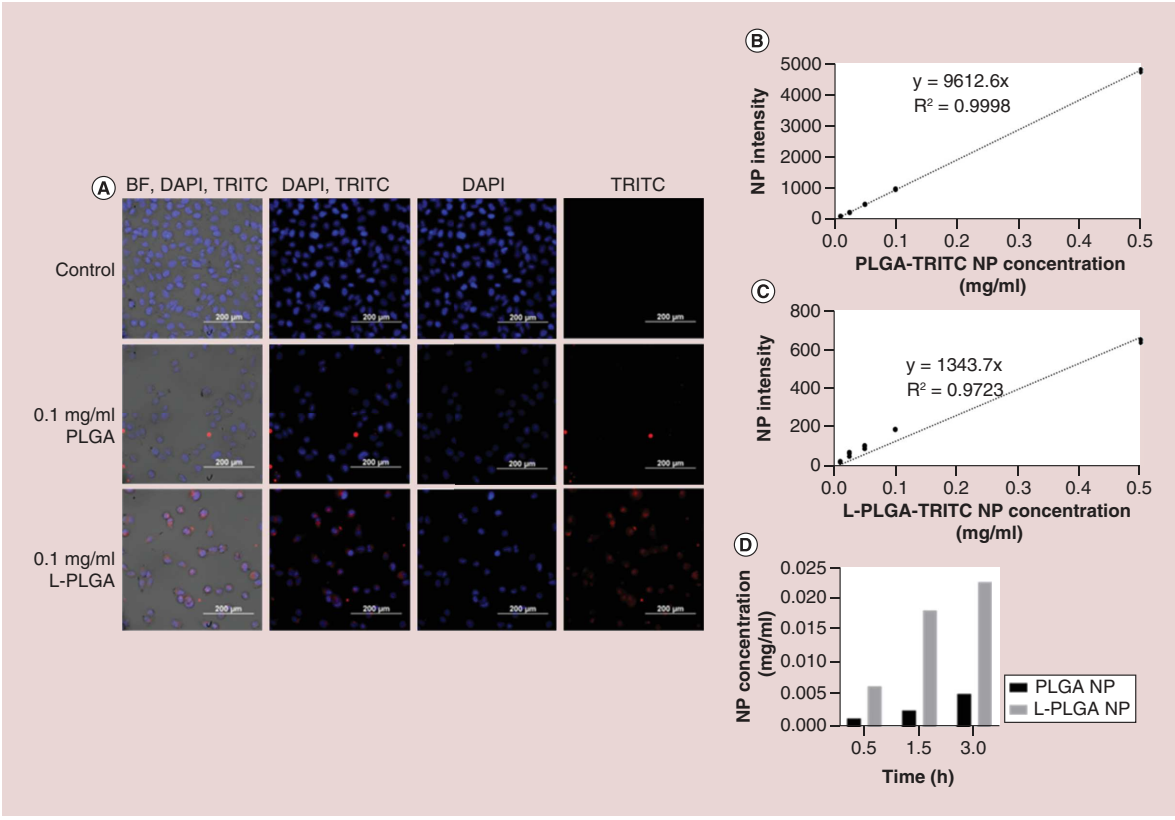

Figure 8. Alkaline-lignin-conjugated-poly(lactic-*co*-glycolic acid) nanoparticles have greater uptake potential than poly(lactic-*co*-glycolic acid) nanoparticles. (A) TNBC cells were seeded on no. 1.5 glass coverslip dishes and cultured for 24 h. The cells were either untreated (control) or treated with fluorescent PLGA-TRITC NPs or L-PLGA-TRITC NPs at 0.1 mg/ml for 3 h. Cells were fixed, stained with DAPI and imaged at 40x. Standard curves were generated for **(B)** PLGA-TRITC NPs and **(C)** L-PLGA-TRITC NPs to quantify nanoparticle uptake. **(D)** Cells were treated with PLGA-TRITC and L-PLGA-TRITC NPs for 0.5, 1.5 and 3 h and the particle uptake was analyzed using flow cytometry and graphed as the concentration of NPs in the cells.
L-PLGA NP: Alkaline-lignin-conjugated-poly(lactic-*co*-glycolic acid) nanoparticle; TNBC: Triple-negative breast cancer; TRITC: Tetramethylrhodamine isothiocyanate.

In addition to NP morphology and drug release, cellular uptake is a key characteristic of NP function. Adherence of NPs to cell membranes is an initial step in the process leading to NP uptake or toxicity [50,51]. Synthetic phospholipid bilayers, such as those comprising DPPC, in the form of solution-based vesicles or lipid bilayers on a solid support are frequently used as model cell membranes to interpret the interactions of cells with surfaces [52,53]. By forming a bilayer directly on a coated quartz crystal sensor, QCM-D has been used to investigate the adherence and uptake of NPs to SLBs [54], the structural rearrangement of NPs adsorbed to the SLBs [55] and the disruption of bilayers by NPs [56–58]. Here, the potential interactions of the cells with PLGA and L-PLGA NPs are inferred from the NP's ability to adhere to or to disrupt the SLBs on QCM gold sensors. As interpreted from the Sauerbrey equation (Equation 2), the mass of the bilayer formed on a sensor is proportional to the decrease in an oscillating crystal's resonance frequency (Δf) [41,43,44]. The QCM-D response of the energy dissipation (ΔD) describes the variation in the viscoelasticity or rigidity of the film coated on the surface [57]. High values of dissipation are the result of deformation of a soft film, whereas low dissipation describes films that are nondeformable and rigid. In relation to SLBs, an increase in dissipation indicates the loosening or thickening of the lipid bilayer [46,59]. In the presence of NPs, an increase in dissipation suggests that the particles have adhered to the bilayer, leading to hydrodynamic effects that increase dissipation loss with the surrounding medium [60]. While the L-PLGA NPs adhered to the model cell membranes, PLGA NPs caused membrane disruption and removal. The distinctly different behaviors of PLGA NPs and L-PLGA NPs with SLBs may be related to the difference in their size as well as surface properties. Larger polymeric NPs are more likely to be engulfed by a bilayer than smaller NPs, leading to mass loss and membrane disruption upon removal [57]. Thus, the smaller size of L-PLGA NPs (92 ± 3.7 nm) as compared with

PLGA (223 ± 1 nm) would favor their penetration into the lipid bilayer rather than disruption [64,65]. Similarly, the effect of functionalized PLGA NPs size on their uptake by Caco-2 cells, a human colon adenocarcinoma cell line, is observed to be 1.3-fold greater for 100 nm NPs compared with 500 nm particles, and about 1.8-fold greater compared with 1000 nm particles [64]. Additionally, the surface chemistry of the polymeric NPs may play a role in the nature of their interaction with the lipid membranes. L-PLGA NPs are stabilized by surface AL, whereas PLGA NPs are stabilized by the addition of PVA, which may impact interactions with lipid bilayers [66]. Cellular uptake of PLGA NPs and modified PLGA NPs is well documented [27,34,36,73–75]. The conjugation of AL, to PLGA produced a much smaller particle with different surface properties, leading to an increase in NP uptake. This increased uptake is what we believe to be responsible for improved efficacy of the L-PLGA nanodelivered GDC-0623 compared with free drug and PLGA entrapped drug.

TNBC is especially difficult to treat because it lacks extracellular targets. Additionally, intracellular drug targeting presents its own set of challenges such as cellular uptake and efflux pumping [76]. The use of NPs is pivotal to increasing the efficacy of targeted therapies for promising intracellular pathways. The MDA-MB-231 cell line was selected as a model for this study because of its mutation causing upregulation of the KRAS pathway [21]. Other studies have achieved successful outcomes using GDC-0623 in cell lines with KRAS mutations because the compound binds to S212 in MEK, which prevents phosphorylation [77,78]. Upregulation of ERK1/2 in breast cancer cells has been shown to induce a more aggressive phenotype through induction of EMT [79]. Nontransformed human epithelial mammary cell line MCF-10A with induced mutations to have ectopic expression of ERK2 demonstrated increased EMT through FRA1 regulation downstream of ERK2. These mutated cells had reduced expression of CDH1 and increased expression of VIM [80]. L-PLGA-GDC NPs exhibited a greater reduction in expression of EMT genes suggest that L-PLGA NPDDS improved the inhibitory effects of free GDC-0623 and PLGA-entrapped GDC-0623. To the best of our knowledge, our lab is the first to report that GDC-0623 reverses EMT in the MDA-MB-231 cell line when administered in free and nanodelivered form.

Conclusion

GDC-0623 did not perform well in a Phase I clinical trial due to having a short-terminal half-life of only 4–6 h following oral dosing [13]. Polymeric NPDDSs have been shown time and time again to improve the pharmacokinetics of cancer therapies, especially with regard to absorption, bioavailability, plasma circulation time and increasing the drug's mean half-life [81–86]. Grafting lignin to PLGA decreased the size of the NPs and improved cellular of uptake. Our novel lignin-based NPDDS demonstrated that we were able to improve the efficacy of GDC-0623 in multiple *in vitro* assays to treat TNBC with KRAS mutations.

Summary points

- Commonly used targeted therapies that act on hormone receptors and are better tolerated by the body than chemotherapies cannot be used to treat triple-negative breast cancer.
- The targeted therapy GDC-0623 did not perform well in a Phase I clinical trial because of poor pharmacokinetics.
- Alkaline-lignin-grafted-poly(lactic-*co*-glycolic acid) (L-PLGA) nanoparticles (NPs) are less than half the size of PLGA NPs, have a better drug-release profile and are more effective at reducing the number of breast cancer cells.
- GDC-0623 is better at inhibiting MEK1/2 activity when entrapped in L-PLGA NPs and delivered to cells.
- GDC-0623 efficacy was improved due to increased cellular uptake of L-PLGA NPs.

Supplementary data

To view the supplementary data that accompany this paper please visit the journal website at: www.futuremedicine.com/doi/suppl/10.2217/nnm-2020-0010

Author contributions

The manuscript was written through contributions of all authors. All the authors have given approval to the final version of the manuscript.

Financial & competing interests disclosure

This work was supported by the National Science Foundation under NSF EPSCoR Track 2 RII, OIA 1632854; the USDA National Institute of Food and Agriculture, AFRI project #2017-07878; the USDA National Institute of Food and Agriculture, AFRI project

#2018-07406; USDA-NIFA Hatch #1008750; and the National Science Foundation, CBET 1509713. The authors have no other relevant affiliations or financial involvement with any organization or entity with a financial interest in or financial conflict with the subject matter or materials discussed in the manuscript apart from those disclosed.

No writing assistance was utilized in the production of this manuscript.

References

Papers of special note have been highlighted as: • of interest; •• of considerable interest

1. Breastcancer.org. Breast cancer information and support. www.breastcancer.org/
2. Berry DA, Cirrincione C, Henderson IC *et al.* Estrogen-receptor status and outcomes of modern chemotherapy for patients with node-positive breast cancer. *JAMA* 295(14), 1658–1667 (2006).
3. Higgins MJ, Baselga J. Targeted therapies for breast cancer. *J. Clin. Invest.* 121(10), 3797–3803 (2011).
4. O'Rorke MA, Murray LJ, Brand JS, Bhoo-Pathy N. The value of adjuvant radiotherapy on survival and recurrence in triple-negative breast cancer: a systematic review and meta-analysis of 5507 patients. *Cancer Treat. Rev.* 47, 12–21 (2016).
5. Hershman DL, Till C, Wright JD *et al.* Comorbidities and risk of chemotherapy-induced peripheral neuropathy among participants 65 years or older in Southwest Oncology Group clinical trials. *J. Clin. Oncol.* 34(25), 3014–3022 (2016).
6. Chao C, Page JH, Yang SJ, Rodriguez R, Huynh J, Chia VM. History of chronic comorbidity and risk of chemotherapy-induced febrile neutropenia in cancer patients not receiving G-CSF prophylaxis. *Ann. Oncol.* 25(9), 1821–1829 (2014).
7. Bradshaw PT, Stevens J, Khankari N, Teitelbaum SL, Neugut AI, Gammon MD. Cardiovascular disease mortality among breast cancer survivors. *Epidemiology* 27(1), 6–13 (2016).
8. de Boer-Dennert M, de Wit R, Schmitz PI *et al.* Patient perceptions of the side-effects of chemotherapy: the influence of 5HT3 antagonists. *Br. J. Cancer* 76(8), 1055–1061 (1997).
9. Tan KX, Danquah MK, Sidhu A, Ongkudon CM, Lau SY. Towards targeted cancer therapy: aptamer or oncolytic virus? *Eur. J. Pharm. Sci.* 96, 8–19 (2017).
10. Zajac M, Muszalska I, Jelinska A. New molecular targets of anticancer therapy – current status and perspectives. *Curr. Med. Chem.* 23(37), 4176–4220 (2016).
11. Oldham RK, Dillman RO. Monoclonal antibodies in cancer therapy: 25 years of progress. *J. Clin. Oncol.* 26(11), 1774–1777 (2008).
12. Iannello A, Ahmad A. Role of antibody-dependent cell-mediated cytotoxicity in the efficacy of therapeutic anti-cancer monoclonal antibodies. *Cancer Metastasis Rev.* 24(4), 487–499 (2005).
13. El-Khoueiry A, Kurkjian C, Semrad T *et al.* Abstract B75: a first in-human Phase I study to evaluate the MEK1/2 inhibitor GDC-0623 in patients with advanced solid tumors. *Mol. Cancer Ther.* 12(Suppl. 11), B75–B75 (2013).
14. Heidorn SJ, Milagre C, Whittaker S *et al.* Kinase-dead BRAF and oncogenic RAS cooperate to drive tumor progression through CRAF. *Cell* 140(2), 209–221 (2010).
15. Rajalingam K, Schreck R, Rapp UR Albert S. RAS oncogenes and their downstream targets. *Biochim. Biophys. Acta* 1773(8), 1177–1195 (2007).
16. Bos JL. RAS oncogenes in human cancer: a review. *Cancer Res.* 49(17), 4682–4689 (1989).
17. Singh H, Longo DL, Chabner BA. Improving prospects for targeting RAS. *J. Clin. Oncol.* 33(31), 3650–3659 (2015).
18. Sale MJ, Cook SJ. Intrinsic and acquired resistance to MEK1/2 inhibitors in cancer. *Biochem. Soc. Trans.* 42(4), 776–783 (2014).
19. Adeyinka A, Nui Y, Cherlet T, Snell L, Watson PH, Murphy LC. Activated mitogen-activated protein kinase expression during human breast tumorigenesis and breast cancer progression. *Clin. Cancer Res.* 8(6), 1747–1753 (2002).
20. Thomas RS, Sarwar N, Phoenix F, Coombes RC, Ali S. Phosphorylation at serines 104 and 106 by Erk1/2 MAPK is important for estrogen receptor-alpha activity. *J. Mol. Endocrinol.* 40(4), 173–184 (2008).
21. Kim R-K, Suh Y, Yoo K-C *et al.* Activation of KRAS promotes the mesenchymal features of basal-type breast cancer. *Exp. Mol. Med.* 47, e137 (2015).
22. Hay M, Thomas DW, Craighead JL, Economides C, Rosenthal J. Clinical development success rates for investigational drugs. *Nat. Biotechnol.* 32(1), 40–51 (2014).
23. Blagosklonny MV. Overcoming limitations of natural anticancer drugs by combining with artificial agents. *Trends Pharmacol. Sci.* 26(2), 77–81 (2005).
24. Liu D, Auguste DT. Cancer targeted therapeutics: from molecules to drug delivery vehicles. *J. Control. Rel.* 219, 632–643 (2015).
25. Suh MS, Shen J, Kuhn LT, Burgess DJ. Layer-by-layer nanoparticle platform for cancer active targeting. *Int. J. Pharm.* 517(1–2), 58–66 (2017).
26. Gao J, Zhong W, He J *et al.* Tumor-targeted PE38KDEL delivery via PEGylated anti-HER2 immunoliposomes. *Int. J. Pharm.* 374(1–2), 145–152 (2009).

27. Cerqueira BBS, Lasham A, Shelling AN, Al-Kassas R. Development of biodegradable PLGA nanoparticles surface engineered with hyaluronic acid for targeted delivery of paclitaxel to triple negative breast cancer cells. *Mater. Sci. Eng. C Mater. Biol. Appl.* 76, 593–600 (2017).
28. Blanco E, Shen H, Ferrari M. Principles of nanoparticle design for overcoming biological barriers to drug delivery. *Nat. Biotechnol.* 33(9), 941–951 (2015).
29. Danhier F, Feron O, Préat V. To exploit the tumor microenvironment: passive and active tumor targeting of nanocarriers for anti-cancer drug delivery. *J. Control. Rel.* 148(2), 135–146 (2010).
30. Bae YH. Drug targeting and tumor heterogeneity. *J. Control. Rel.* 133(1), 2–3 (2009).
31. Folkman J. Angiogenesis in cancer, vascular, rheumatoid and other disease. *Nat. Med.* 1(1), 27–31 (1995).
32. Matsumura Y, Maeda H. A new concept for macromolecular therapeutics in cancer chemotherapy: mechanism of tumoritropic accumulation of proteins and the antitumor agent smancs. *Cancer Res.* 46(12 Pt 1), 6387–6392 (1986).
33. Maeda H, Bharate GY, Daruwalla J. Polymeric drugs for efficient tumor-targeted drug delivery based on EPR-effect. *Eur. J. Pharm. Biopharm.* 71(3), 409–419 (2009).
34. Sims LB, Curtis LT, Frieboes HB, Steinbach-Rankins JM. Enhanced uptake and transport of PLGA-modified nanoparticles in cervical cancer. *J. Nanobiotechnol.* 14, 33 (2016).
35. Klapiszewski Ł, Zdarta J, Antecka K *et al.* Magnetite nanoparticles conjugated with lignin: a physicochemical and magnetic study. *Appl. Surf. Sci.* 422, 94–103 (2017).

• **Lignin conjugated to magnetite nanoparticles improved thermal and electrokinetic properties.**

36. Liu K, Zheng D, Lei H *et al.* Development of novel lignin-based targeted polymeric nanoparticle platform for efficient delivery of anticancer drugs. *ACS Biomater. Sci. Eng*. 4(5), 1730–1737 (2018).

•• **Alkaline lignin was conjugated to folic acid-polyethylene glycol to make a novel nanoparticle drug-delivery systems. The nanoparticle drug-delivery systems improved the efficacy of the targeted therapy hydroxyl camptothecin.**

37. Wang X, Zhou X, Hecht SM. Role of the 20-hydroxyl group in camptothecin binding by the topoisomerase I-DNA binary complex. *Biochemistry* 38(14), 4374–4381 (1999).
38. Muse ES, Patel NR, Astete CE, Damann KE, Sabliov CM. Surface association and uptake of poly(lactic-co-glycolic) acid nanoparticles by *Aspergillus flavus*. *Ther. Deliv.* 5(11), 1179–1190 (2014).
39. Tabaei SR, Choi J-H, Haw Zan G, Zhdanov VP, Cho N-J. Solvent-assisted lipid bilayer formation on silicon dioxide and gold. *Langmuir* 30(34), 10363–10373 (2014).
40. Cho N-J, Frank CW, Kasemo B, Höök F. Quartz crystal microbalance with dissipation monitoring of supported lipid bilayers on various substrates. *Nat. Protoc.* 5(6), 1096–1106 (2010).
41. Patel AR, Frank CW. Quantitative analysis of tethered vesicle assemblies by quartz crystal microbalance with dissipation monitoring: binding dynamics and bound water content. *Langmuir* 22(18), 7587–7599 (2006).
42. Evans K. Supported phospholipid bilayer interaction with components found in typical room-temperature ionic liquids – a QCM-D and AFM study. *Int, J. Mol. Sci.* 9(4), 498–511 (2008).
43. Andersson M, Sellborn A, Fant C, Gretzer C, Elwing H. Acoustics of blood plasma on solid surfaces. *J. Biomater. Sci. Polym. Ed.* 13(8), 907–917 (2002).
44. Santos-Martinez MJ, Inkielewicz-Stepniak I, Medina C *et al.* The use of quartz crystal microbalance with dissipation (QCM-D) for studying nanoparticle-induced platelet aggregation. *Int. J. Nanomedicine* 7, 243–255 (2012).
45. Lind TK, Cárdenas M. Understanding the formation of supported lipid bilayers via vesicle fusion-a case that exemplifies the need for the complementary method approach (review). *Biointerphases* 11(2), 020801 (2016).
46. Joshi T, Voo ZX, Graham B, Spiccia L, Martin LL. Real-time examination of aminoglycoside activity towards bacterial mimetic membranes using Quartz Crystal Microbalance with dissipation monitoring (QCM-D). *Biochim. Biophys. Acta* 1848(2), 385–391 (2015).
47. Lesniak A, Salvati A, Santos-Martinez MJ, Radomski MW, Dawson KA, Åberg C. Nanoparticle adhesion to the cell membrane and its effect on nanoparticle uptake efficiency. *J. Am. Chem. Soc.* 135(4), 1438–1444 (2013).
48. Shpigel N, Levi MD, Sigalov S, Daikhin L, Aurbach D. *In situ* real-time mechanical and morphological characterization of electrodes for electrochemical energy storage and conversion by electrochemical quartz crystal microbalance with dissipation monitoring. *Acc. Chem. Res.* 51(1), 69–79 (2018).
49. Sadman K, Wiener CG, Weiss RA, White CC, Shull KR, Vogt BD. Quantitative rheometry of thin soft materials using the quartz crystal microbalance with dissipation. *Anal. Chem.* 90(6), 4079–4088 (2018).
50. Chen KL, Bothun GD. Nanoparticles meet cell membranes: probing nonspecific interactions using model membranes. *Environ. Sci. Technol.* 48(2), 873–880 (2014).
51. Yousefi N, Tufenkji N. Probing the Interaction between nanoparticles and lipid membranes by quartz crystal microbalance with dissipation monitoring. *Front. Chem.* 4, 46 (2016).

52. Chen Q, Xu S, Liu Q, Masliyah J, Xu Z. QCM-D study of nanoparticle interactions. *Adv. Colloid Interface Sci.* 233, 94–114 (2016).
53. Tong X, Moradipour M, Novak B *et al.* Experimental and molecular dynamics simulation study of the effects of lignin dimers on the gel-to-fluid phase transition in DPPC bilayers. *J. Phys. Chem. B.* 123(39), 8247–8260 (2019).
54. Ábrahám Á, Katona M, Kasza G, Kiss É. Amphiphilic polymer layer – model cell membrane interaction studied by QCM and AFM. *Eur. Polym. J.* 93, 212–221 (2017).
55. Frost R, Grandfils C, Cerda B, Kasemo B, Svedhem S. Structural rearrangements of polymeric insulin-loaded nanoparticles interacting with surface-supported model lipid membranes. *J. Biomater. Nanobiotechnol.* 2(2), 180–192 (2011).
56. Zhao F, Holmberg JP, Abbas Z *et al.* TiO_2 nanoparticle interactions with supported lipid membranes – an example of removal of membrane patches. *RSC Adv.* 6(94), 91102–91110 (2016).
57. Bailey CM, Kamaloo E, Waterman KL, Wang KF, Nagarajan R, Camesano TA. Size dependence of gold nanoparticle interactions with a supported lipid bilayer: a QCM-D study. *Biophys. Chem.* 203–204, 51–61 (2015).
58. Jing B, Zhu Y. Disruption of supported lipid bilayers by semihydrophobic nanoparticles. *J. Am. Chem. Soc.* 133(28), 10983–10989 (2011).
59. Reimhult K, Yoshimatsu K, Risveden K, Chen S, Ye L, Krozer A. Characterization of QCM sensor surfaces coated with molecularly imprinted nanoparticles. *Biosens. Bioelectron.* 23(12), 1908–1914 (2008).
60. Tellechea E, Johannsmann D, Steinmetz NF, Richter RP, Reviakine I. Model-independent analysis of QCM data on colloidal particle adsorption. *Langmuir* 25(9), 5177–5184 (2009).
61. Hasan IY, Mechler A. Formation of planar unilamellar phospholipid membranes on oxidized gold substrate. *Biointerphases* 11(3), 031017 (2016).
62. Zwang TJ, Fletcher WR, Lane TJ, Johal MS. Quantification of the layer of hydration of a supported lipid bilayer. *Langmuir* 26(7), 4598–4601 (2010).
63. Marquês JT, Viana AS, de Almeida RFM. A biomimetic platform to study the interactions of bioelectroactive molecules with lipid nanodomains. *Langmuir* 30(42), 12627–12637 (2014).
64. Win KY, Feng S-S. Effects of particle size and surface coating on cellular uptake of polymeric nanoparticles for oral delivery of anticancer drugs. *Biomaterials* 26(15), 2713–2722 (2005).
65. Qaddoumi MG, Ueda H, Yang J, Davda J, Labhasetwar V, Lee VHL. The characteristics and mechanisms of uptake of PLGA nanoparticles in rabbit conjunctival epithelial cell layers. *Pharm. Res.* 21(4), 641–648 (2004).
66. Sahoo SK, Panyam J, Prabha S, Labhasetwar V. Residual polyvinyl alcohol associated with poly(D,L-lactide-co-glycolide) nanoparticles affects their physical properties and cellular uptake. *J. Control. Rel.* 82(1), 105–114 (2002).
67. Uttamsingh S, Bao X, Nguyen KT *et al.* Synergistic effect between EGF and TGF-beta1 in inducing oncogenic properties of intestinal epithelial cells. *Oncogene* 27(18), 2626–2634 (2008).
68. Gujral TS, Chan M, Peshkin L, Sorger PK, Kirschner MW, MacBeath G. A noncanonical Frizzled2 pathway regulates epithelial-mesenchymal transition and metastasis. *Cell* 159(4), 844–856 (2014).
69. Casalino L, De Cesare D, Verde P. Accumulation of Fra-1 in RAS-transformed cells depends on both transcriptional autoregulation and MEK-dependent posttranslational stabilization. *Mol. Cell. Biol.* 23(12), 4401–4415 (2003).
70. Astete CE, Sabliov CM. Synthesis and characterization of PLGA nanoparticles. *J. Biomater. Sci. Polym. Ed.* 17(3), 247–289 (2006).

•• **Presents a comprehensive review of poly(lactic-*co*-glycolic acid) (L-PLGA) nanoparticle (NP) synthesis methods and parameters that govern particle characteristics.**

71. Noguchi T, Yamamuro T, Oka M *et al.* Poly(vinyl alcohol) hydrogel as an artificial articular cartilage: evaluation of biocompatibility. *J. Appl. Biomater.* 2(2), 101–107 (1991).
72. Xu A, Yao M, Xu G *et al.* A physical model for the size-dependent cellular uptake of nanoparticles modified with cationic surfactants. *Int. J. Nanomedicine* 7, 3547–3554 (2012).
73. Cartiera MS, Johnson KM, Rajendran V, Caplan MJ, Saltzman WM. The uptake and intracellular fate of PLGA nanoparticles in epithelial cells. *Biomaterials* 30(14), 2790–2798 (2009).

•• **Fluorescent PLGA NPs were used to explore cellular uptake and intracellular fate in three different epithelial cell lines.**

74. Bao W, Liu R, Wang Y *et al.* PLGA-PLL-PEG-Tf-based targeted nanoparticles drug delivery system enhance antitumor efficacy via intrinsic apoptosis pathway. *Int. J. Nanomedicine* 10, 557–566 (2015).

• **Modified PLGA NPs improved the efficacy of chemotherapy daunorubicin using *in vivo* xenograft models.**

75. Davda J, Labhasetwar V. Characterization of nanoparticle uptake by endothelial cells. *Int. J. Pharm.* 233(1–2), 51–59 (2002).
76. Kirtane AR, Kalscheuer SM, Panyam J. Exploiting nanotechnology to overcome tumor drug resistance: challenges and opportunities. *Adv. Drug Deliv. Rev.* 65(13–14), 1731–1747 (2013).
77. Hatzivassiliou G, Haling JR, Chen H *et al.* Mechanism of MEK inhibition determines efficacy in mutant KRAS- versus BRAF-driven cancers. *Nature* 501(7466), 232–236 (2013).

- **There are differences in constitutive MAPK pathway activation depending on whether it is KRAS or BRAF driven. These differences should be considered when designing drugs to target that pathway through MEK inhibition.**

78. Zaanan A, Okamoto K, Kawakami H, Khazaie K, Huang S, Sinicrope FA. The mutant KRAS gene up-regulates BCL-XL protein via STAT3 to confer apoptosis resistance that is reversed by BIM protein induction and BCL-XL antagonism. *J. Biol. Chem.* 290(39), 23838–23849 (2015).
79. Shin S, Blenis J. ERK2/Fra1/ZEB pathway induces epithelial-to-mesenchymal transition. *Cell Cycle* 9(13), 2483–2484 (2010).
80. Shin S, Dimitri CA, Yoon S-O, Dowdle W, Blenis J. ERK2 but not ERK1 induces epithelial-to-mesenchymal transformation via DEF motif-dependent signaling events. *Mol. Cell.* 38(1), 114–127 (2010).
81. Khalil NM, do Nascimento TCF, Casa DM *et al.* Pharmacokinetics of curcumin-loaded PLGA and PLGA-PEG blend nanoparticles after oral administration in rats. *Colloids Surf. B Biointerface.* 101, 353–360 (2013).
82. Xie X, Tao Q, Zou Y *et al.* PLGA nanoparticles improve the oral bioavailability of curcumin in rats: characterizations and mechanisms. *J. Agric. Food Chem.* 59(17), 9280–9289 (2011).
83. Alexis F, Pridgen E, Molnar LK, Farokhzad OC. Factors affecting the clearance and biodistribution of polymeric nanoparticles. *Mol. Pharm.* 5(4), 505–515 (2008).
84. Kumari A, Yadav SK, Yadav SC. Biodegradable polymeric nanoparticles based drug delivery systems. *Colloids Surf. B Biointerfaces* 75(1), 1–18 (2010).
85. Masood F. Polymeric nanoparticles for targeted drug delivery system for cancer therapy. *Mater. Sci. Eng. C Mater. Biol. Appl.* 60, 569–578 (2016).
86. Khalil NM, Carraro E, Cótica LF, Mainardes RM. Potential of polymeric nanoparticles in AIDS treatment and prevention. *Expert Opin. Drug Deliv.* 8(1), 95–112 (2011).